Effect of Ta addition on the electrochemical behavior and functional fatigue life of metastable Ti-Zr-Nb based alloy for indwelling implant applications

M.F. Ijaz [a], Y. Zhukova [a, *], A. Konopatsky [a], S. Dubinskiy [a], A. Korobkova [a], Y. Pustov [a], V. Brailovski [b], S. Prokoshkin [a]

[a] National University of Science and Technology "MISIS", 4 Leninskiy Prosp, Moscow 119049, Russia
[b] Ecole de Technologie Superieure, 1100, Rue Notre Dame Ouest, Montreal, H3C 1K3, Canada

ABSTRACT

In this paper, the effects of Ta substitution for Nb, on the microstructure and corrosion fatigue behavior of metastable Ti-18Nb-14Zr biomedical alloy are investigated for the first time. For this purpose, besides previously studied ternary Ti-18Zr-14Nb alloy, new quaternary Ti-18Zr-13Nb-1Ta (at.%) biomedical alloy was also synthesized by vacuum arc remelting method and subjected to thermomechanical treatment processes. The *in situ* electrochemical behavior and subsequent functional fatigue life of both alloys showed a strong dependence on the composition and microstructure. The electrochemical results from the test bench demonstrated that during monotonic cycling the fatigue life of Ta-added alloy was significantly longer than that of the Ti-18Zr-14Nb alloy. Thus, the addition of Ta to the ternary Ti-18Zr-14Nb alloy was found to be very effective in increasing the resistance to fatigue degradation mainly by exhibiting excellent protective passivation tendency. Based on the electrochemical evaluation and fractrographic characteristics, it is concluded that the combined effect of the stable passive film formation and higher development of a nanosubgrained structure in β phase results in the prolonged fatigue life of Ta-added alloy.

© 2018 Elsevier B.V. All rights reserved.

1. Introduction

Ti-Ni based alloys are one of the most distinctive families of superelastic alloys, which provide myriad advantages in the diverse engineering domains [1,2]. At present, the superior functional fatigue properties of superelastic Ti-Ni based alloys have been commercially exploited in the manufacturing of various indwelling implants such as endovascular stents, catheter guide wire, dental braces, etc. [1–3]. Unfortunately, the risks of the hypersensitivity associated with Ti-Ni-based alloys due to the release of Ni ions from corrosion reactions against the human body have also been significantly identified [2–6].

Over the years, in order to establish greater efficacy of the biomedical implants, several Ni-free biomedical superelastic alloys had been exquisitely elaborated as a replacement for the conventional Ti-Ni based alloys [4–16]. Among them, multicomponent

metastable β-type Ti-Nb- [2–4,6,9,11–13,17–20] and Ti-Zr- [4,7,10] based alloys, with different β-stabilizing element substitutions are most prevalent in the biomedical field.

Typically, the superelastic effect in metastable β-Ti alloy is derived from the reversible stress-induced martensitic transformation during the mechanical loading-unloading cycling [3,5,9,15]. Some factors affecting cyclic fatigue properties, like nanoscale concentration modulation inducing confinement of the martensitic transformation, have been described recently in Refs. [20–22].

For this reason, the evaluation of functional fatigue life under monotonous mechanical cycling is of pivotal significance [3,5,15,16,23].

Recently, it has been reported that the addition of Ta as a substitute for Nb in Ti-18Nb-14Zr alloy is a promising way to further improve the functional fatigue properties of Ti-Zr-Nb based superelastic alloys [24]. Undoubtedly, the metastable β-type ternary Ti-Zr-Nb [4,10] and/or quaternary Ti-Zr-Nb-Ta base alloys, are beginning to emerge as the latest research frontiers in

biomedical applications [4,10,24].

Yet surprisingly, according to our knowledge, none of the studies have been meticulously conducted to characterize the *in situ* corrosion functional fatigue performance and fracture characteristics of Ti-Zr-Nb alloy.

In this line of thought, from a practical viewpoint, it would be very enticing to synergistically elucidate and compare the effects of alloying substitutions i.e., Ta on the electrochemical behavior and the functional fatigue life of newly developed Ti-18Zr-14Nb alloy in the adverse physiological environments [5,25,26].

For this purpose, we have recently built and validated a prototype electrochemical test bench which emulates the *in vitro* conditions to which the wire-shaped implants will be actually subjected *in vivo* [27,28].

2. Materials and methods

The Ti-18Zr-13Nb-1Ta and Ti-18Zr-14Nb at. % alloys ingots (all compositions are hereafter referred in atomic percent) were prepared by the vacuum arc-melting method with a consumable electrode. In order to ensure the chemical homogeneity of the alloys, each ingot was remelted several times and flipped before each melting step. Each ingot was sliced in to 1.5 mm thick plates using electric discharge machining. Next, the rectangular shaped plates were homogenized at 1173 K for 1.8 ks under Ar atmosphere, followed by rapid quenching in water. Afterward, all the plates were subjected to thermomechanical treatments (TMT). The TMT included the following; cold rolling with a true logarithmic strain of $e = 0.3$ and post-deformation annealing at 873 K for 1.8 ks followed by water quenching. The post-deformation annealing at 873 K (1.8 ks) creates a nanosubgrained structure in the beta-phase of the studied alloys [24] which provides the best combination of functional properties of analogous alloys [15]. After the annealing, all the thermomechanically treated specimen were mechanically polished by fine abrasive paper P1200 to minimize the surface effect. The dimensions of the sheet-shaped specimens for fatigue testing were ~0.5 mm in thickness and ~3 mm in width, with a gauge length of ~120 mm. A long length of the specimen was selected in order to reduce the unnecessary grip pressure, thereby decreasing the stress accumulation at the end of the wedges. In addition, longer length of the specimen is also beneficial to establish optimum electrolytic contact during cycling. Microstructural investigations were conducted using *Versamet-2 Union* metallographic optical microscope and *JEOL 2100* transmission electron microscope (TEM) at 200 keV. TEM grids with a diameter of 3 mm were punched from the sheet with a consistent thermomechanical treatment [24]. TEM specimens were polished and thinned down to 100 μm then exposed to Ar ion bombardment thinning using a *Precision Ion Polishing System*. In order to evaluate the average

functional fatigue life, the room temperature fatigue tests on all the thermomechanically treated specimens were performed while utilizing the specially designed pseudo-physiological test bench [28]. In the context of the present study, the term of functional fatigue actually stands for strain-controlled low cycle fatigue in simulated physiological conditions, because it is the advanced way to assess the functional behavior of the real implants. During each fatigue cycle, the strain (bending) amplitude was maintained at 1.5%. At the same time, the electrochemical behavior of both alloys during the fatigue test was also monitored by open circuit potential measurements (OCP) using *IPC Pro MF* potentiostat (*Volta Co*, Russia), against a reference saturated silver chloride electrode (Ag/AgCl) (RE). During fatigue cycling, the gauge length of the specimens was acting as working electrode (WE). The specimens were immersed simultaneously and tested in physiological Hank's solution containing (concentrations, g/l): 8 NaCl, 0.4 KCl, 0.04 Na_2HPO_4, 0.06 KH_2PO_4, 0.2 $MgSO_4 \cdot 7H_2O$, 0.35 $NaHCO_3$, 0.14 $CaCl_2$, H_2O (up to 1 L of solution), pH 7.4. The electrochemical measurements were carried out in both steady state and dynamic-cycling state. At least five samples of each alloy were tested under the same conditions. The construction and the operating principle of the electrochemical test bench have already been explained elsewhere [28].

Finally, *Vegas-Tescan* scanning electron microscope (SEM) observation was used to analyze the different region of fatigue fracture.

3. Results and discussion

3.1. Microstructure of Ti-18Zr-14Nb and Ti-18Zr-13Nb-1Ta alloys

The optical microscopy study was carried out for the purpose of grain size comparison of both alloys before TMT. Typical grain structures are shown in Fig. 1. It follows from Fig. 1 that the alloys possess approximately the same grain size (100−500 μm) which points to the fact that Ta for Nb substitution of 1 at.% does not affect initial grain structure of the material.

In order to discuss the effect of TMT on the microstructure of Ti-18Zr-14Nb and Ti-18Zr-13Nb-1Ta alloys, the TEM study was performed. Fig. 2 shows the TEM bright and dark field images with the corresponding selected-area diffraction patterns (shown in insets) with a beam parallel to [113]β of Ti-18Zr-14Nb and Ti-18Zr-13Nb-1Ta alloys. The corresponding dark field images for both specimens (as shown in Fig. 2b and d) were obtained using the (110) type reflection of the β-phase which is the main phase in both alloys. The bright and dark field images shown in Fig. 2 reveal that after the thermomechanical treatment both specimens consist of a polygonized dislocation substructure, with high dislocation density inside subgrains (indicated by white arrows in Fig. 2b and d). Note that this type of substructure formation has also been observed in
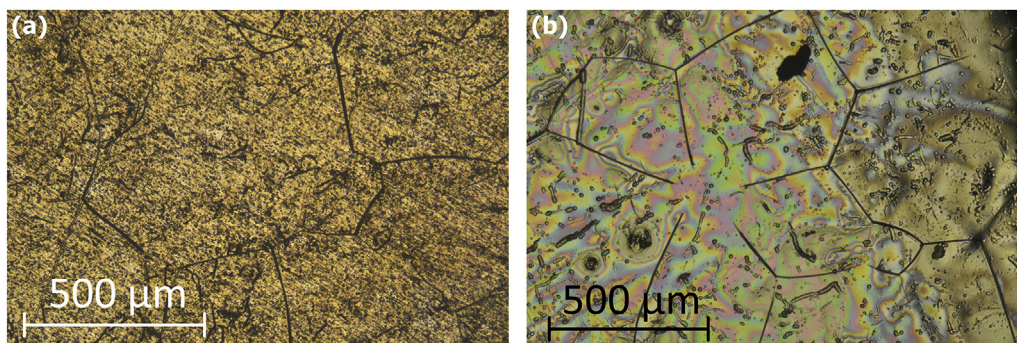

Fig. 1. Optical microscopy images of as-cast Ti-18Zr-14Nb (a) and Ti-18Zr-13Nb-1Ta (b) alloys' grain structure.
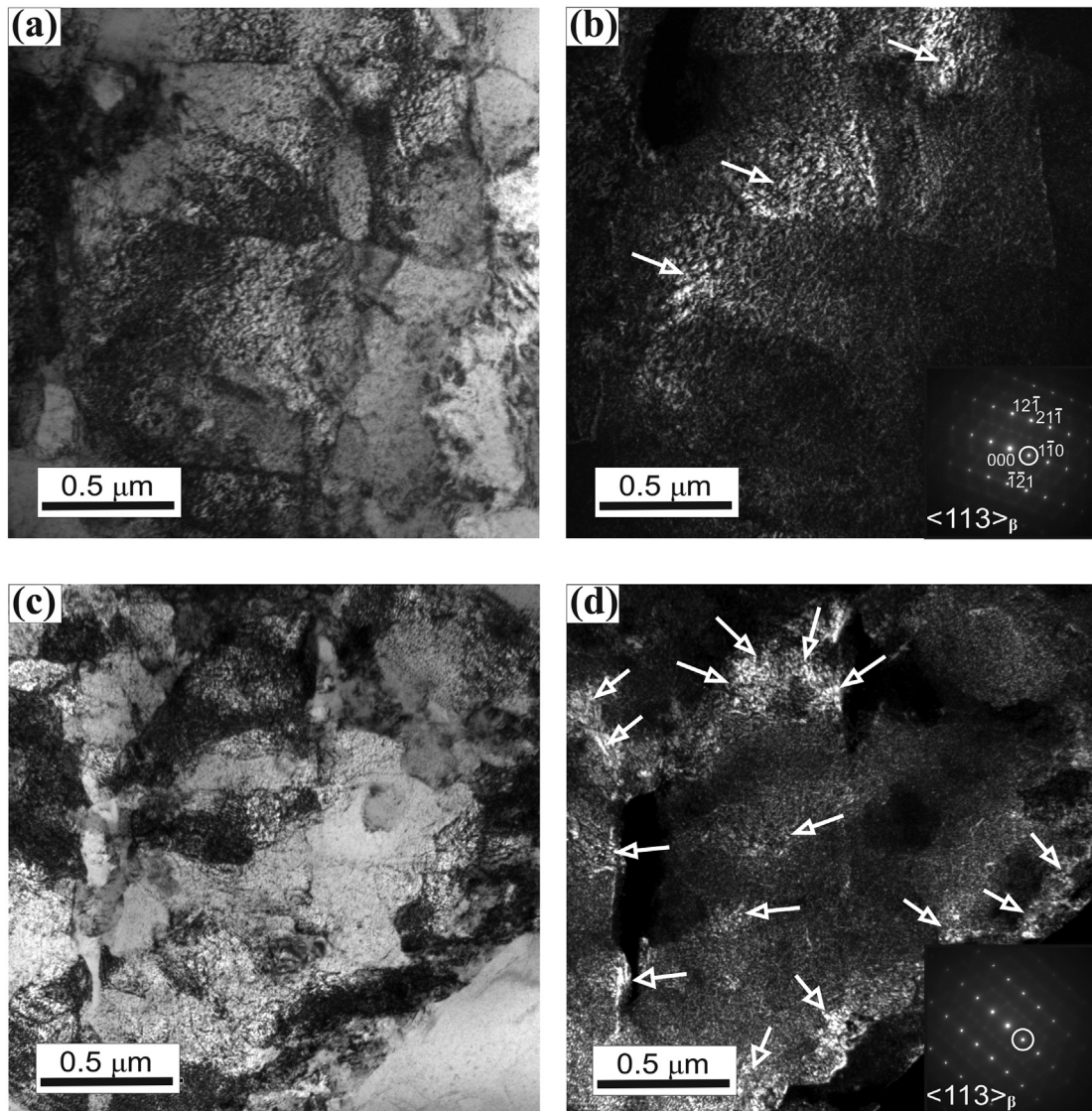
Fig. 2. Transmission electron microscopy bright and dark field images with a selected-area-diffraction pattern (shown in inset) for (a–b) Ti-18Zr-14Nb and (c–d) Ti-18Zr-13Nb-1Ta alloy specimen before the functional fatigue cycling in Hank's solution.

Ti-Ni, Ti-Nb-Zr and Ti-Nb-Ta based alloys [5,9,24]. While comparing both the images, following comparative observations may be of interest. According to the obtained diffraction contrast images, Ti-18Zr-13Nb-1Ta alloy tends to demonstrate more developed sub-grained structure after TMT with somewhat smaller subgrain size compared to Ti-18Zr-14Nb (Fig. 2). Apparently, the formation of smaller subgrains in Ti-18Zr-13Nb-1Ta alloy is ascribable to lower diffusion coefficient of Ta in the β structure which, consequently, led to the slower subgrain growth [5]. Nonetheless, the subgrain size of Ti-18Zr-13Nb-1Ta and Ti-18Zr-14Nb alloys occupies rather wide ranges of 50–500 and 100–600 nm, respectively. For that reason, more in-depth statistical analysis of large amount of TEM images is needed in order to evaluate the influence of Ta for Nb substitution on the features of subgrains structure.

3.2. Electrochemical behavior of studied materials during functional fatigue cycling

Fig. 3 displays the open circuit potential (OCP) values (mV) as a function of exposure time (s) for the Ti-18Zr-14Nb and Ti-18Zr-13Nb-1Ta alloy specimens subjected to functional fatigue cycling in Hank's solution. The summary of the experimental results is also illustrated in Table 1. Prior to functional fatigue cycling the respective time-invariant steady states (E_{st}) for both the alloys was established. The E_{st} value of Ti-18Zr-14Nb alloy (-118 mV) is slightly lower than that of Ti-18Zr-13Nb-1Ta (-76 mV). Once, the respective E_{st} for both the specimens was achieved the functional fatigue cycling with a constant bending strain of 1.5% was imposed. Firstly, it can be identified that after the initiation of cycling the OCP for both Ti-18Zr-14Nb and Ti-18Zr-13Nb-1Ta alloy specimens shifted towards the negative values. Nonetheless, the shifts in the OCP towards negative potentials are associated to the abrupt cathodic polarizations [25–32]. Indeed, the E_c values for the Ti-18Zr-14Nb and Ti-18Zr-13Nb-1Ta alloy are about -453 and -588 mV respectively.

Although, at the initial stage of fatigue cycling, the shift in ΔE towards negative values is larger in case of Ti-18Zr-13Nb-1Ta alloy specimen when compared to Ti-18Zr-14Nb alloy specimen (as shown in Fig. 3(a and b)) respectively. However, as the cycling proceeded, the E_c of Ti-18Zr-13Nb-1Ta alloy specimen exhibits

(a)

(Ti-18Zr-14Nb)
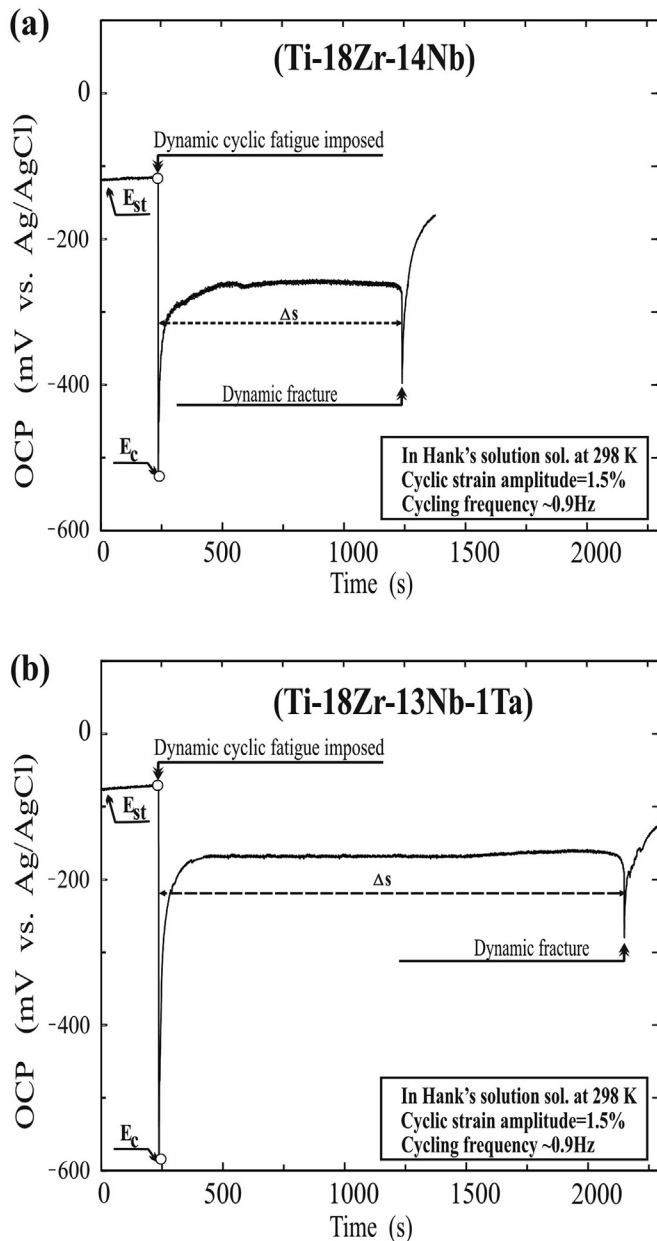
(b)

(Ti-18Zr-13Nb-1Ta)

Fig. 3. Typical OCP curves acquired during the functional fatigue cycling of (a) Ti-18Zr-14Nb and (b) Ti-18Zr-13Nb-1Ta alloy specimen while applying constant 1.5% bending strain in Hank's solution (the OCP drop at the moment of cycling start is marked with circles ○).

increasing tendency with the time duration for about 400 s and then keeps stable and higher OCP values during the entire cycling (as shown in Fig. 3b).

It is because the protective passive films once forms begin to

Table 1
Comparison of the results from functional fatigue cycling of the Ti-18Zr-14Nb and Ti-18Zr-13Nb-1Ta alloys in Hank's solution.

Alloy	Average number of cycles to failure (N_{max})	Open circuit potential (mV) (Ag/AgCl)		
		E_{st}	E_c	$\Delta E_{(Est-Ec)}$
Ti-18Zr-14Nb	854 ± 328	−118	−453	−335
Ti-18Zr-13Nb-1Ta	1806 ± 559	−76	−588	−512

grow on the Ti-18Zr-13Nb-1Ta alloy specimen surface and then forms a stable and strong passive film during the cycling. The higher protective ability of the surface film on Ti-18Zr-13Nb-1Ta alloy can be attributed to Ta^{5+} ions favourable dissolution in TiO_2 matrix film as compared to Zr^{4+} ions due to closer ionic radii (0.064, 0.066 and 0.082 nm for Ti^{4+}, Ta^{5+} and Zr^{4+}, respectively) resulting in lower point defect concentration and, consequently, the stability is increased.

Another reason, for this stable passive film formation, might be due to the "chemomechanical effect" which is elicited at the specimen/electrolyte interface [27–29].

In other words, during the functional fatigue cycling unlike to Ti-18Zr-14 Nb alloy, the surface of the Ti-18Zr-13Nb-1Ta alloy specimen is more defiant to the impact of cycling.

Accordingly, it can be deduced that the substitution of Ta for Nb in Ti-18Zr-14Nb alloy has resulted in the formation of a stable passive film, which in return can successfully mitigate the corrosion fatigue damage.

On the other hand, at the dynamic fracture stage for both the specimens a slight but distinct negative shift typically corresponding to fracture was observed which was finally followed by a rapid recovery in the positive direction in the OCP plots owing to passivation of the freshly formed surface [27,28]. Thus, the negative shift in the OCP values is essentially due to the local rupture of the protective film and/or due to the dissolution of the film prevailing over its formation [25–27].

The dynamic fracture for the specimens during functional fatigue cycling was estimated to occur around 1500 s for Ti-18Zr-14Nb and 2300 s for Ti-18Zr-13Nb-1Ta alloy specimen.

Eventually, while comparing the corresponding average functional fatigue life of Ti-18Zr-14Nb and Ti-18Zr-13Nb-Zr-1Ta alloy specimens, which in our case is defined as the total number of successful loading-unloading cycles (N_{max}) which a specimen can withstand before dynamic fracture. The N_{max} for Ti-18Zr-14Nb and Ti-18Zr-13Nb-1Ta alloy specimens in the physiological solution is calculated to be 854 ± 328 and 1806 ± 559 cycles respectively. Note that the N_{max} values obtained in low-cycle fatigue tests of analogous Ti-Nb-Zr-Sn alloys were much higher (over 50000 cycles) [17–19] at comparable maximum strain in a cycle. The reason for this difference is the difference in the experimental conditions of the present and reference investigations, including differences in surface roughness, sample size and dimensions, straining modes, thermomechanical conditions of tests, thermomechanical treatment modes and corresponding microstructures of alloys.

In order to discuss the longer functional fatigue lifetime of Ti-18Zr-13Nb-1Ta alloy in the physiological solution, the apparent surface components of the fracture surfaces of Ti-18Zr-14Nb and Ti-18Zr-13Nb-1Ta alloy specimens were systematically studied.

3.3. Fractography of fractured specimen after fatigue test in physiological solution

Fig. 4 shows the general fractography of Ti-18Zr-14Nb and Ti-18Zr-13Nb-1Ta alloy specimens, which was characterized by SEM. The precise comparison of the macroscopic and microscopic regions for Ti-18Zr-14Nb and Ti-18Zr-13Nb-1Ta alloy specimens, particularly the crack origin (noted by white arrows), fatigue striations region and a final unstable region which is nearby the dynamic fractured area are also illustrated in Fig. 4a and b respectively. On the other hand, for the sake of clarity, the segment of fatigue striations by the crack propagation in the stable region and dimples at the unstable region for both Ti-18Zr-14Nb and Ti-18Zr-13Nb-1Ta alloy specimens alloy are also highlighted with the white delineated rectangular boxes.

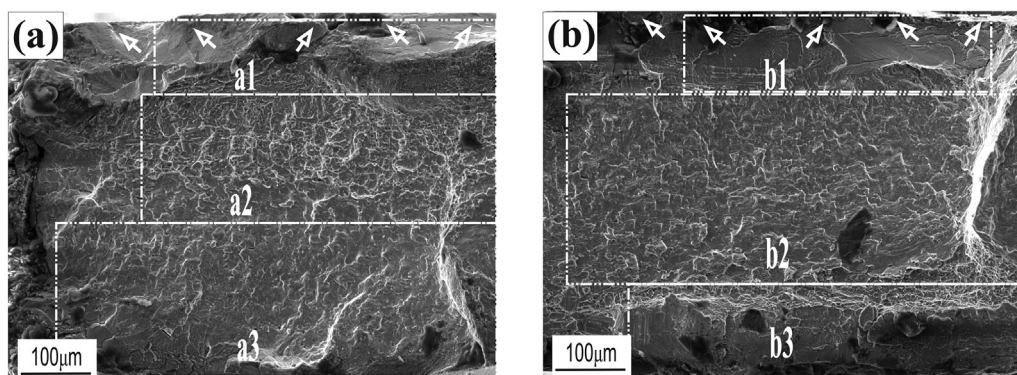From general aspects, it is evident that the dynamic fracture in

Fig. 4. Typical SEM fractographs showing the comparison of the overall fracture surfaces of (a) Ti-18Zr-14Nb and (b) Ti-18Zr-13Nb-1Ta alloys with special focus on different observable fatigue fracture mechanisms: *a1, b1* – fatigue crack origin and propagation region; *a2, b2* – fatigue striations at the stable growth region; *a3, b3* – fatigue stripes and dimples at the unstable region.

both of the specimen was elicited mainly by trans-granular pattern [23,28,32] as the corresponding three regions shown in Fig. 4 are easily identifiable. Particularly, it is also noteworthy that in the case of Ti-18Zr-14Nb the stable region showing the fatigue crack propagation is much smaller than the final overloaded region. In fact, the enlarged unstable zone of Ti-18Zr-14Nb alloy (Fig. 4a) on one hand corroborates the lower fatigue life of Ti-18Zr-14Nb alloy. It is presumably because the local passive films breakage during cycling loading has accelerated the corrosion-assisted fatigue crack growth which collectively has led in the increase in the length of the final unstable region when compared to the fatigue striations region (Fig. 4a).

Unlikely, the fractography of the Ti-18Zr-13Nb-1Ta alloy specimen (Fig. 4b) clearly indicates a much larger fatigue striation region when compare to Ti-18Zr-14Nb alloy specimen (Fig. 4a). During cycling, the fatigue striations streaks on the specimen surface are assumed to be generated by the successive opening and/or closing of the surface cracks. The lengths of fatigue striation region can substantially influence the functional fatigue lifetime of an implant [28].

Additionally, the peculiarities of the reversible martensitic transformation β ↔ α″ underlying the superelasticity effect in these alloys may influence the features of the fracture surfaces [33].

Thus, by correlating the microstructural results with the OCP response it is suggested that the increase in the functional fatigue lifetime of Ti-18Zr-13Nb-1Ta alloy is firstly related to the to the stable passive film formation which inhibits the local corrosive attack (as shown in Fig. 3b).

Meanwhile, while complementing these findings, with the stabilized OCP response of Ti-18Zr-13Nb-1Ta alloy specimen (Fig. 4b), it is claimed that the relatively higher mechanical strength of Ti-18Zr-13Nb-1Ta alloy which was due to the formation of nano-subgrained structure (as shown in Fig. 2b) can also be an additional and/or contributing factor for the longer functional fatigue lifetime of Ti-18Zr-13Nb-1Ta specimen. It is because during functional fatigue cycling the greater difference between dislocation and transformation yield stresses has also resulted in the prolonged functional fatigue life of Ti-Nb-based alloys [5,9,22,24].

4. Conclusions

The effects of Ta content on the microstructure, electrochemical behavior and fatigue life of Ti-Nb-Zr alloy were investigated after thermomechanical treatment in the custom-made pseudo-physiological test bench. The experimental results are summarized as follows:

1. The substitution of Ta for Nb promotes more developed subgrain structure and changes the subgrain size of thermomechanically treated Ti-18Zr-14Nb alloy towards the nanometer scale.
2. The Ti-18Zr-13Nb-1Ta alloy exhibited higher open circuit potential values during cycling and its passive oxide film is found to be more stable and adequately resistant to the impact of functional fatigue when compared to Ti-18Zr-14Nb alloy.
3. Substitution of 1% Nb by Ta increases functional fatigue life almost twice: $N_{max} = 1806$ for Ti-18Zr-13Nb-1Ta in contrast with $N_{max} = 854$ for Ti-18Zr-14Nb alloy.
4. Based on the fractographic characteristics and electrochemical evaluation, it is concluded that beside the stable passive film formation on the specimen surface, the combined effect of the unique β phase nanosubgrained structure also contributes to the prolonged fatigue life of Ti-18Zr-13Nb-1Ta alloy.

References

[1] T. Duerig, A. Pelton, D. Stockel, An overview of nitinol medical applications, Mater. Sci. Eng. 273–275 (1999) 149–160.
[2] T. Yoneyama, S. Miyazaki, Shape Memory Alloys for Biomedical Applications, Woodhead Publishing, Cambridge, 2009.
[3] M. Niinomi, Mechanical biocompatibilities of titanium alloys for biomedical applications, J. Mech. Beh. Biomed. Mater 1 (2008) 30–42.
[4] H.Y. Kim, J. Fu, H. Tobe, J.I. Kim, S. Miyazaki, Crystal structure, transformation strain, and superelastic property of Ti–Nb–Zr and Ti–Nb–Ta alloys, Shap. Mem. Superelasticity 1 (2015) 107–116.
[5] S.D. Prokoshkin, V. Brailovski, A.V. Korotitskiy, K. Inaekyan, S.M. Dubinskiy, M.R. Filonov, M.I. Petrzhik, Formation of nanostructures in thermomechanically treated Ti–Ni and Ti–Nb–(Zr, Ta) SMAs and their roles in martensite crystal lattice changes and mechanical behavior, J. Alloy. Comp. 577S (2013) 418–422.
[6] H.Y. Kim, S. Hashimoto, J.I. Kim, T. Inamura, H. Hosoda, S. Miyazaki, Effect of Ta addition on shape memory behavior of Ti–22Nb alloy, Mat. Sci. and Eng. A 417 (2006) 120–128.
[7] M.F. Ijaz, H.Y. Kim, H. Hosoda, S. Miyazaki, Superelastic properties of biomedical (Ti-Zr)-Mo-Sn alloys, Mater. Sci. Eng. C 48 (2015) 11–20.
[8] M.F. Ijaz, D. Laille, L. Heraud, D.M. Gordin, P. Castany, T. Gloriant, Design of a novel superelastic Ti-23Hf-3Mo-4Sn biomedical alloy combining low modulus, high strength and large recovery strain, Mater. Lett. 177 (2016)

39–41.

[9] S. Prokoshkin, V. Brailovski, S. Dubinsky, Y. Zhukova, V. Sheremetyev, A. Konopatsky, K. Inaekyan, Manufacturing, structure control, and functional testing of Ti–Nb-Based SMA for medical application, Shap. Mem. Superelasticity 2 (2016) 130–144.

[10] J. Fu, H.Y. Kim, S. Miyazaki, Effect of annealing temperature on microstructure and superelastic properties of a Ti-18Zr-4.5Nb-3Sn-2Mo alloy, J. Mech. Behav. Biomed 65 (2017) 716–723.

[11] M.F. Ijaz, H.Y. Kim, H. Hosoda, S. Miyazaki, Effect of Sn addition on stress hysteresis and superelastic properties of a Ti–15Nb–3Mo alloy, Scripta Mater. 72–73 (2014) 29–32.

[12] P. Castany, A. Ramarolahy, F. Prima, P. Laheurte, C. Curfs, T. Gloriant, In situ synchrotron X-ray diffraction study of the martensitic transformation in superelastic Ti-24Nb-0.5N and Ti-24Nb-0.5O alloys, Acta Mater. 88 (2015) 102–111.

[13] E. Bertrand, T. Gloriant, D.M. Gordin, E. Vasilescu, P. Drob, C. Vasilescu, S.I. Drob, Synthesis and characterization of a new superelastic Ti-25Ta-25Nb biomedical alloy, J Mech Behav Biomed Mater. 3 (2010) 559–564.

[14] Y. Al-Zain, H.Y. Kim, H. Hosoda, T.H. Nam, S. Miyazaki, Shape memory properties of Ti–Nb–Mo biomedical alloys, Acta Mater. 58 (2010) 4212–4223.

[15] V. Sheremetyev, V. Brailovski, S. Prokoshkin, K. Inaekyn, S. Dubinskiy, Functional fatigue behavior of superelastic beta Ti-22Nb-6Zr (at%) alloy for load-bearing biomedical applications, Mater. Sci. Eng. C 58 (2016) 935–944.

[16] S.J. Li, T.C. Cui, Y.L. Hao, R. Yang, Fatigue properties of a metastable β-type titanium alloy with reversible phase transformation, Acta Biomater. 4 (2008) 305–317.

[17] S.Q. Zhang, S.J. Li, M.T. Jia, F. Prima, L.J. Chen, Y.L. Hao, R. Yang, Low-cycle fatigue properties of a titanium alloy exhibiting nonlinear elastic deformation behavior, Acta Mater. 59 (11) (2011) 4690–4699.

[18] S.J. Li, M.T. Jia, F. Prima, Y.L. Hao, R. Yang, Improvements in nonlinear elasticity and strength by grain refinement in a titanium alloy with high oxygen content, Scripta Mater. 64 (11) (2011) 1015–1018.

[19] Z.B. Zhang, Y.L. Hao, S.J. Li, R. Yang, Fatigue behavior of ultrafine-grained Ti–24Nb–4Zr–8Sn multifunctional biomedical titanium alloy, Mater. Sci. Eng. 577 (2013) 225–233.

[20] Y.L. Hao, H.L. Wang, T. Li, J.M. Cairney, A.V. Ceguerra, Y.D. Wang, …, R. Yang, Superelasticity and tunable thermal expansion across a wide temperature range, J. Mater. Sci. Technol. 32 (8) (2016) 705–709.

[21] H.L. Wang, Y.L. Hao, S.Y. He, T. Li, J.M. Cairney, Y.D. Wang, …, S.J. Li, Elastically confined martensitic transformation at the nano-scale in a multifunctional titanium alloy, Acta Mater. 135 (2017) 330–339.

[22] H.L. Wang, Y.L. Hao, S.Y. He, K. Du, T. Li, E.G. Obbard, …, F. Prima, Tracing the coupled atomic shear and shuffle for a cubic to a hexagonal crystal transition, Scripta Mater. 133 (2017) 70–74.

[23] C. Fleck, D. Eifler, Corrosion, fatigue and corrosion-fatigue behavior of metal implant materials, Int. J. Fatig. 32 (2010) 929–935.

[24] A.S. Konopatsky, S. Dubinskiy, Y. Zhukova, V. Sheremetyev, V. Brailovski, S. Prokoshkin, M.R. Filonov, Ternary Ti-Zr-Nb and quaternary Ti-Zr-Nb-Ta shape memory alloys for biomedical applications: Structural features and cyclic mechanical properties, Mater. Sci. Eng. 702 (2017) 301–311.

[25] E.M. Gutman, Mechanochemistry of Materials, Cambridge International Science Publishing, 1998.

[26] Y.S. Zhukova, Y.A. Pustov, A.S. Konopatsky, M.R. Filonov, Characterization of electrochemical behavior and surface oxide films on superelastic biomedical Ti–Nb–Ta alloy in simulated physiological solutions, J. Alloy. Comp. 586 (2014) s535–s538.

[27] Y.S. Zhukova, Y.A. Pustov, A.S. Konopatsky, M.R. Filonov, S.D. Prokoshkin, Electrochemical behavior of novel superelastic biomedical alloys in simulated physiological media under cyclic load, J. Mater. Eng. Perform. 23 (2014) 2677–2681.

[28] M.F. Ijaz, S. Dubinskiy, Y. Zhukova, A. Korobkova, Y. Pustov, V. Brailovski, S. Prokoshkin, Novel electrochemical test bench for evaluating the functional fatigue life of biomedical alloys, JOM (J. Occup. Med.) 69 (2017) 1334–1339.

[29] L. Qiang, L. Junjie, M. Guanghao, L. Xuyan, P. Deng, Influence of ω phase precipitation on mechanical performance and corrosion resistance of Ti–Nb–Zr alloy, Mater. Des. 111 (2016) 421–428.

[30] Y. Bai, S.J. Li, F. Prima, Y.L. Hao, R. Yang, Electrochemical corrosion behavior of Ti-24Nb-4Zr-8Sn alloy in a simulated physiological environment, Appl. Surf. Sci. 258 (2012) 4035–4040.

[31] R. Ion, S.I. Drob, M.F. Ijaz, C. Vasilescu, P. Osiceanu, D.M. Gordin, A. Cimpean, T. Gloriant, Surface characterization, corrosion resistance and in vitro biocompatibility of a new Ti-Hf-Mo-Sn alloy, Materials 9 (2016) 818.

[32] ASTM F 1801–1997, Standard Practice for Corrosion Fatigue Testing of Metallic Implant Material, 2004.

[33] Y.A. Pustov, Y.S. Zhukova, M.R. Filonov, The role of martensitic transformation in corrosion fatigue failure of Ti–22Nb–6Ta and Ti–22Nb–6Zr (at %) medical alloys, Protect. Met. Phys. Chem. Surface 50 (2014) 524–529.